Article

Study on the Mechanical Response Mechanism and Damage Behavior of a Tunnel Lining Structure under Reverse Fault Dislocation

Huifeng Su *, Zhongxiao Zhao, Kun Meng and Shuo Zhao

College of Transportation, Shandong University of Science and Technology, Qingdao 266590, China
* Correspondence: skd991970@sdust.edu.cn

Abstract: In this paper, the mechanical response mechanism and damage behavior of a railway tunnel lining structure under reverse fault dislocation were studied. The damage behavior of railway tunnel linings under reverse fault dislocation was validated by undertaking laboratory tests and three-dimensional numerical simulations, where Coulomb's friction was used in the tangential direction of the interface. The failure damage, which increasingly accumulates with displacements, mainly concentrates in fault fracture neighborhoods 0.5 D to 1.5 D (D is the tunnel diameter) within the footwall. The maximum surrounding rock pressure and the maximum longitudinal strain develop in the tunnel near the hanging wall area. The damage begins as longitudinal cracking of the inverted arch. With the increase in dislocations, those cracks develop upward to the arch foot and the waist. Consequently, those oblique cracks separate lining segments, leading to abutment dislocation. The research results provide technical guidance and theoretical support for on-site construction and follow-up research, and they have important application value.

Keywords: reverse fault dislocation; railway tunnel; model test; numerical simulation; lining response

1. Introduction

1.1. Research Background and Significance

During tunnel construction, faults of different scales will inevitably be encountered and are the main geological disasters affecting the safety of the project. The influence of fault dislocation on the tunnel has various characteristics, such as anisotropy and complexity. Previously, it was generally believed that the tunnel is a relatively stable structure constrained by the surrounding geotechnical media, and the proportion of damage will be very low if an earthquake occurs. Therefore, except for special cases, it was generally believed that an earthquake would have little impact on the tunnel structure. The indoor similar model test along with three-dimensional numerical simulation is a good method to study such problems.

For some complex structures in which the mathematical models for the relevant physical quantities have not been established or are difficult to establish, model tests can often achieve better results. It is difficult to accurately describe the damage of the tunnel lining structure under the action of reverse faults by mathematical methods. Moreover, due to the unpredictability of the dislocation, field observation is greatly limited, and it is difficult to obtain comprehensive data. Although the model test simplifies some aspects, it still has advantages that other methods cannot match in terms of the phenomenon laws and other data studied. This chapter takes a railway tunnel crossing with an active reverse fault as the prototype. We determined the scale by combining the existing devices and materials, and we found the appropriate proportion of similar materials through orthogonal tests. The damage behavior of the tunnel lining structure under reverse fault dislocation was studied by this model test. The longitudinal strain of typical parts of the lining and the contact pressure of the surrounding rock were measured and analyzed, and the distribution and development of lining damage were observed and recorded. The characteristic law of damage behavior evolution of the tunnel lining structure was summarized.

1.2. Research Status

Review, urbanization, resource recovery, waste recovery, and environmental assessment were the top five keywords, and the current research fields were linked with future trends [1,2]. The highway tunnel is one of the primary infrastructure systems affecting community welfare. They are vulnerable to higher deterioration limits, but the funds available for their maintenance and rehabilitation are limited. This situation requires the development of a degradation model to predict the performance state behavior of key tunnel components [3]. The influence of cyclic load, cumulative load, and other loads on buildings is complex and diverse [4,5].

Sun Fengbo et al. [6–8] studied the anti-dislocation mechanism and evaluation method, and they pointed out that the fault dislocation rate is a factor reflecting the strength of fault activity. Various scholars have conducted a large number of model tests on tunnel crossing active faults. Xiao Zhihui [9] pointed out that the fault intersection angle has an important influence on the deformation and failure mechanism of the tunnel near the fault through a model test of the strike slip fault sand layer, and they obtained the relationship between the tunnel strain and the fault when the fault intersection angle is less than 45°. In order to study the influence law of fault tunnels under earthquake action, Liu Yun et al. [10] carried out shaking table comparative tests through fault tunnels, and they found that the development of tunnel lining cracks is closely related to the structural location. The final failure form of the tunnel was composed of longitudinal tensile cracks of the pipe joint itself and the staggered platform at the pipe joint. Liu Xuezeng et al. [11–13] simulated the stress deformation and failure process of the tunnel structure under the stick slip dislocation of normal faults with different dip angles, such as 45°, 60° and 75°, and determined the maximum fault displacement allowed for structural failure, proposed the failure area of the tunnel lining, and determined the shear zone and footwall range. Zhang Yunfei et al. [14] conducted a model test on the influence of fault dislocation on the tunnel across the fault when the geometric similarity ratio was 100 and the fault inclination was 90°. They found that the longitudinal strain distribution law of the tunnel lining arch waist was consistent under different dislocation quantities, and the tunnel lining strain was positively correlated with the dislocation quantity. The strain of the tunnel lining at different plates on both sides of the fracture zone presented an antisymmetric distribution. The maximum strain was located in the fault fracture zone. Baziar et al. [15] studied the structural mechanics and deformation characteristics of tunnel crossing reverse faults in dry sandy soil through centrifuge model tests, and analyzed the action mechanism of fault location, displacement, intersection angle, and other parameters on the tunnel. Kiani et al. [16] carried out normal fault centrifuge model tests with a geometric scale ratio of 1:50 and a fault dip of 60° and 75°, respectively, to study the influence of the fault dip and tunnel depth on the damage of shield tunnels. The research showed that increasing the tunnel depth can effectively reduce the damage of tunnels. Sabagh et al. [17] studied the failure law of fault dislocation and tunnel diameter on the tunnel and surrounding rock through the centrifuge normal fault dislocation test with a geometric scale of 1:60, and qualitatively graded the tunnel damage according to the dislocation and tunnel failure phenomenon. Saiyar [18] carried out a centrifuge model test of cross fault tunnels with a scale of 1/30. The development and evolution of cracks in tunnels under the action of fault dislocation were studied. The correlation between the development of tunnel cracks and the depth and density of overburden was analyzed.

Scholars at home and abroad [19–27] have conducted in-depth research by means of mutual verification, such as model tests and numerical simulation. However, the current research has mainly focused on the macroscopic mechanical and deformation response of fault activity in the tunnel structure, and the research on the damage behavior of the railway tunnel lining structure under reverse fault dislocation is insufficient. Previous studies have mostly focused on the influence of active faults with different dip angles on the tunnel, and there is still no complete analysis of the influence of reverse fault activity on the lining structure of segmental tunnels under different displacements. The longitudinal

strain and the contact pressure between the lining and surrounding rock were measured by simulating the dislocation (creep) of a tunnel passing through an active fault, and the measured parameters were compared and analyzed to obtain the damage evolution law and characteristics of a tunnel passing through an active fault lining structure, to reveal the damage mechanism of the tunnel lining.

1.3. Research Framework Figure

The flow research framework is shown in Figure 1.
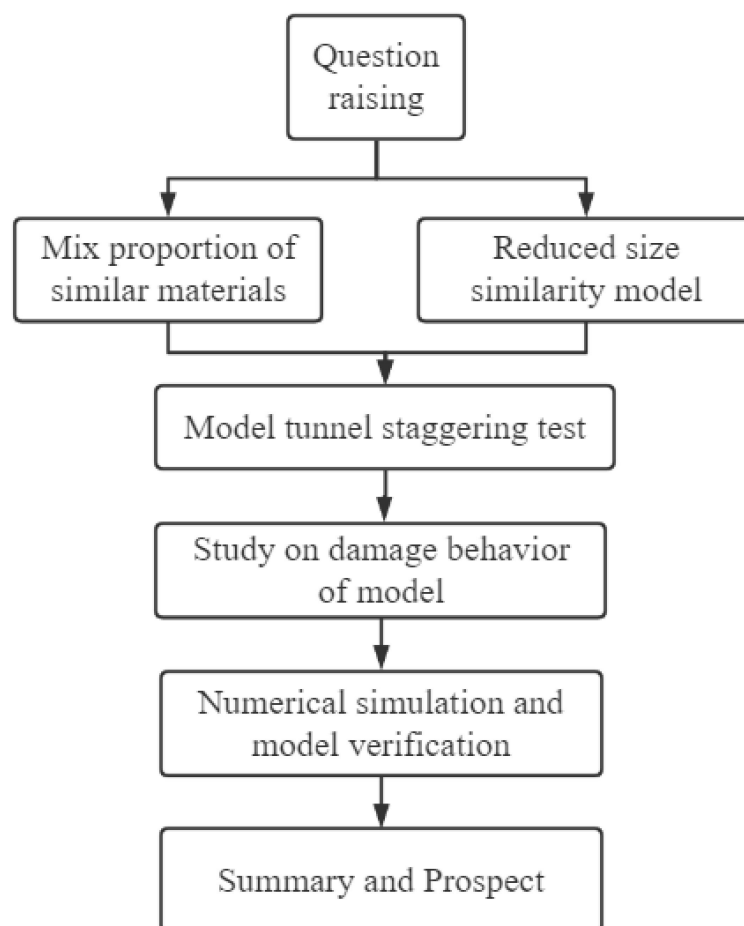
Figure 1. Research framework figure.

2. Model Test

2.1. Test Device

The test device was the existing tunnel crossing active fault dislocation test model box, and the box size (length × width × height) was 2 m × 1 m × 1 m, with a thickness of 4 cm. The fracture zone was mainly located in the footwall. The simulated inclination of the box was 60°, and the intersection angle between the fault and the tunnel was 60°. The model included the upper wall, the lower wall, the reaction wall, the fixed connecting device, and the loading device. The lower wall was fixed to the reaction wall through connecting bolts, and a fixed support was installed on the ground below it, so that it would remain stationary during the test loading process. The hanging wall completed the displacement in the staggered direction through the loading device, so as to realize a more realistic simulation of reverse fault dislocation. The loading device was composed of two sets of jacks, which could be manually controlled to rise and fall at the same time, simulating the deformation rate of reverse fault activity. As shown in Figure 2.
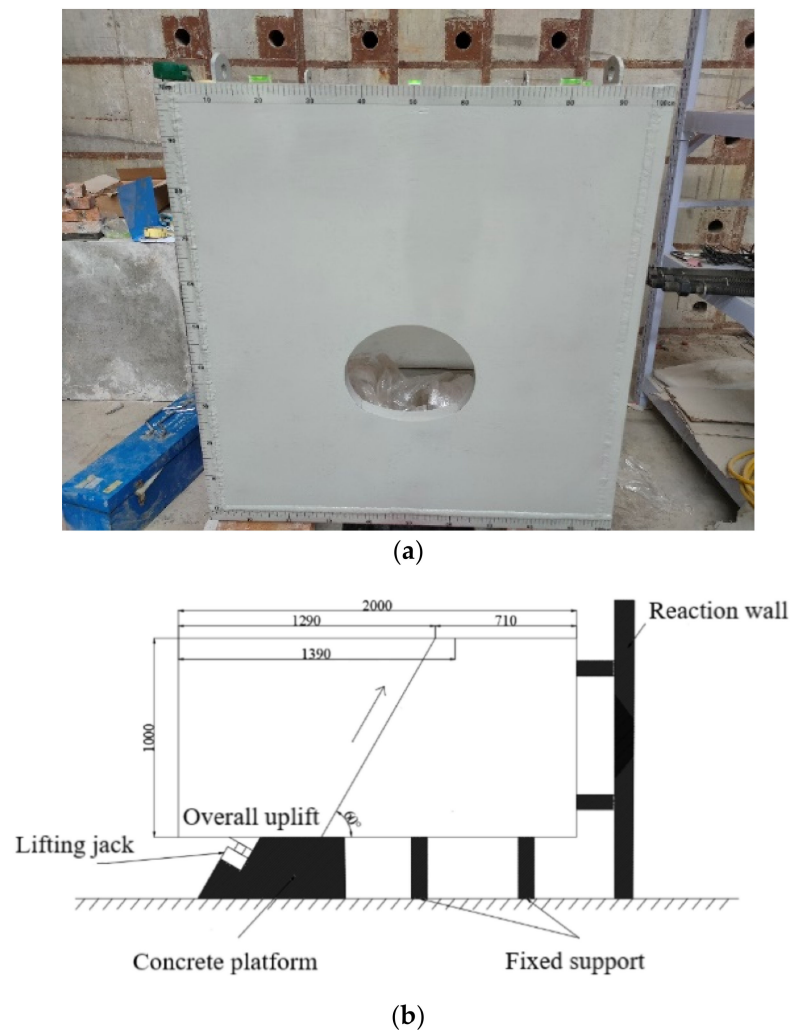
Figure 2. Model diagram: (**a**) Model box device diagram; (**b**) schematic diagram of fault dislocation simulation.

2.2. Similarity Principle and Similarity Ratio

The similarity principle of the model test refers to the physical phenomena in the model corresponding to the physical phenomena of the technical prototype and the properties of the materials. The geometry and load of the model must be similar to the prototype, and the physical quantities between them must correspond to a certain proportion; that is, the order of similarity. According to the basic principles of elasticity and rock mechanics, each point of the model should correspond to the equilibrium equation, coordination equation, and geometric equation. All points on the surface of the model should meet the boundary conditions. The similarity principle can be expressed as: if the model and prototype are two similar systems, their geometric characteristics and physical dimensions must maintain a certain proportional relationship, so as to subtract the corresponding physical quantities of the prototype system from the physical dimensions of the model system.

According to the above principles, combined with the size of the model device and the boundary effect, the geometric similarity ratio of this model test was determined to be 30, and the stress similarity ratio was determined to be 45. Then, the similarity scale of each physical and mechanical parameter was determined, as shown in Table 1. The external dimensions of the tunnel model were determined following this: the height was 29 cm, the width 34 cm, and the thickness 2.4 cm.

Table 1. Similarity relation and scale of main physical quantities.

Physical Quantity	Similarity Relation	Similar Scale
Length l/m	C_l	30
Stress σ/(N/m^2)	C_σ	45
Strain ε	$C_\varepsilon = 1$	1
Poisson's ratio ν	$C_\nu = 1$	1
Internal friction angle φ/(°)	$C_\varphi = 1$	1
Cohesion c/Pa	$C_c = C_\sigma$	45
Modulus of elasticity E/Pa	$C_E = C_\sigma$	45
Density ρ/(kg/m^3)	$C_\sigma = C_E/C_l$	1.5

Limited by the size of the existing test device and considering the size of the measuring elements, the lining size after scaling should not be too small, otherwise it will affect the data measurement. The physical and mechanical parameters of similar materials also have a certain range, so the setting of the basic similarity scale needs to be done carefully. In conclusion, the geometric similarity scale of this model test was set as 30 and the elastic modulus similarity scale was set as 45. According to this similarity relation, the similarity relation of other main physical quantities is determined. The physical and mechanical parameters of the prototype and model were calculated. As shown in Table 2.

Table 2. Material physical and mechanical parameters of prototype and model.

Category	Material Type	Density (kg/m^3)	Modulus of Elasticity E (MPa)	Poisson's Ratio (μ)	Cohesion c (kPa)	Internal Friction Angle (°)
Prototype	wall rock	2100	4500	0.32	500	33
	lining	2500	30,000	0.2	–	–
Model	wall rock	1400	100	0.32	11	33
	lining	1666.67	666.67	0.2	–	–

Considering the limitations of the geometric scale of the model, the primary support and secondary lining were regarded as one, and the material properties referred to C30 concrete. According to the fact that the sliding surface of the active fault often occurs in the middle of the fracture zone, the fault fracture zone was simplified, and only the fracture zone at 6 m near the fault dislocation surface was considered.
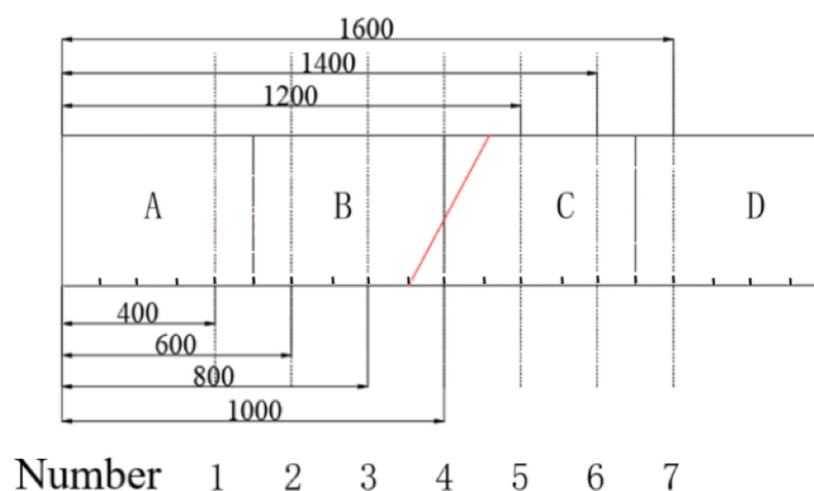
2.3. Similar Materials

We carried out field tests to obtain the basic physical and mechanical parameters of the surrounding rock and lining, and we obtained the physical and mechanical parameters of similar materials through similar scale, as well as carrying out orthogonal tests and comprehensive tests on this basis. In this experiment, the density, elastic modulus, cohesion, and internal friction angle were selected as the main research parameters, and different material proportioning relationships were adjusted to make the model material and prototype material meet the requirements of the similarity ratio. Through a large number of proportioning tests, it was found that when the mass ratio of river sand/fly ash/waste oil was 29:61:10, the density, cohesion, and internal friction angle of the obtained surrounding rock material basically met the requirements of similar ratio, in which the particle size range of river sand was 0~1.5 mm, and the fly ash was class II. In this paper, river sand with a particle size larger than 1.5 mm was used for the simulation. The design parameters of the tunnel lining came from the actual project. Through the proportioning test of concrete materials, a gypsum/water/retarder mass ratio of 1.32:1:0.005 was selected for the proportioning of similar concrete materials. As shown in Table 3.

Table 3. Parameters of the surrounding rock and lining materials.

Parameter	Prototype Value	Model Value	Measured Value	Relative Error
Density $\rho/(\text{kg/m}^3)$	2100~2200	1400~1467	1389	99.2%
Cohesion c/kPa	500	11	11.315	97.1%
Internal friction angle $\varphi/(°)$	33	33	33.11	99.7%
Lining density $\rho/(\text{kg/m}^3)$	2500	1666	1692	98.4%
Elastic modulus of lining E/MPa	28,000	622	635	97.9%

2.4. Test Content

The damage behavior of the tunnel lining structure under reverse fault activity was studied. The main measurement data were surface strain and surrounding rock contact pressure, and the damage and cracking of the lining were observed. For this purpose, a total of seven test sections were set, numbering from the leftmost side of the hanging wall to the rightmost side of the footwall at an interval of 20 cm. The No. 4 test section was located at the fault dislocation surface. Figure 3 shows the distribution of monitoring sections.


Figure 3. Monitoring section distribution map (unit: mm).

The specific steps of the model stagger test are shown in Figure 4.

(1)　We configured similar materials to the surrounding rock, and put raw materials such as river sand, fly ash, and waste engine oil into the mixer according to the ratio determined above to mix evenly.

(2)　Poured the lining model; put the gypsum, water, retarder, and other raw materials into the mixer according to the proportions determined above, mixed them evenly, and poured the lining model in the precast mold. In order to prevent the gypsum from flowing out of the side gap when it is not solidified, gaskets were added at the joint of the external formwork. In order to fix the relative position of the two outer molds, we used screws at the joint of the mold and clamped the screws so that the gasket filled the whole gap. The inner mold could be removed half an hour after pouring. After the gypsum was completely solidified, the outer mold was removed for curing. After the air drying reached sufficient strength, the strain gauge and micro pressure sensor were pasted onto the test section.

(3)　We filled the model box with the configured surrounding rock material. When it was filled to the height of the tunnel, we placed the lining model with the test elements arranged, sorted out and led out the conductors, checked whether they were intact with a multimeter, connected the instruments to test and zero, and then continued to compact the filler to the top of the box. After the work on the model box was completed, we opened the data acquisition instrument and observed whether there were abnormal test elements. If there were abnormal elements, we eliminated the

abnormal conditions before proceeding to the next step. If there was no abnormality, we recorded the initial stress and displacement of the lining model, and then cleared the balance to prepare for the subsequent data collection.

(4) A jack was used to load and lift the hanging wall of the model, so that the hanging wall could maintain displacement along the direction of the sliding surface to simulate the fault activity. The vertical displacement rate of the hanging wall was taken as 1 mm/min, and every 5 mm was a stage, with periodic dislocations of 5 mm, 10 mm, 15 mm, 20 mm, 25 mm, and 30 mm for 30 min, respectively. We collected and recorded the data of each monitoring element at this time. After the vertical stagger distance reached 30 mm, it did not stop periodically, and continued to load and lift until the model was seriously damaged.

(5) After the test, we excavated the lining structure, and observed and recorded its damage.
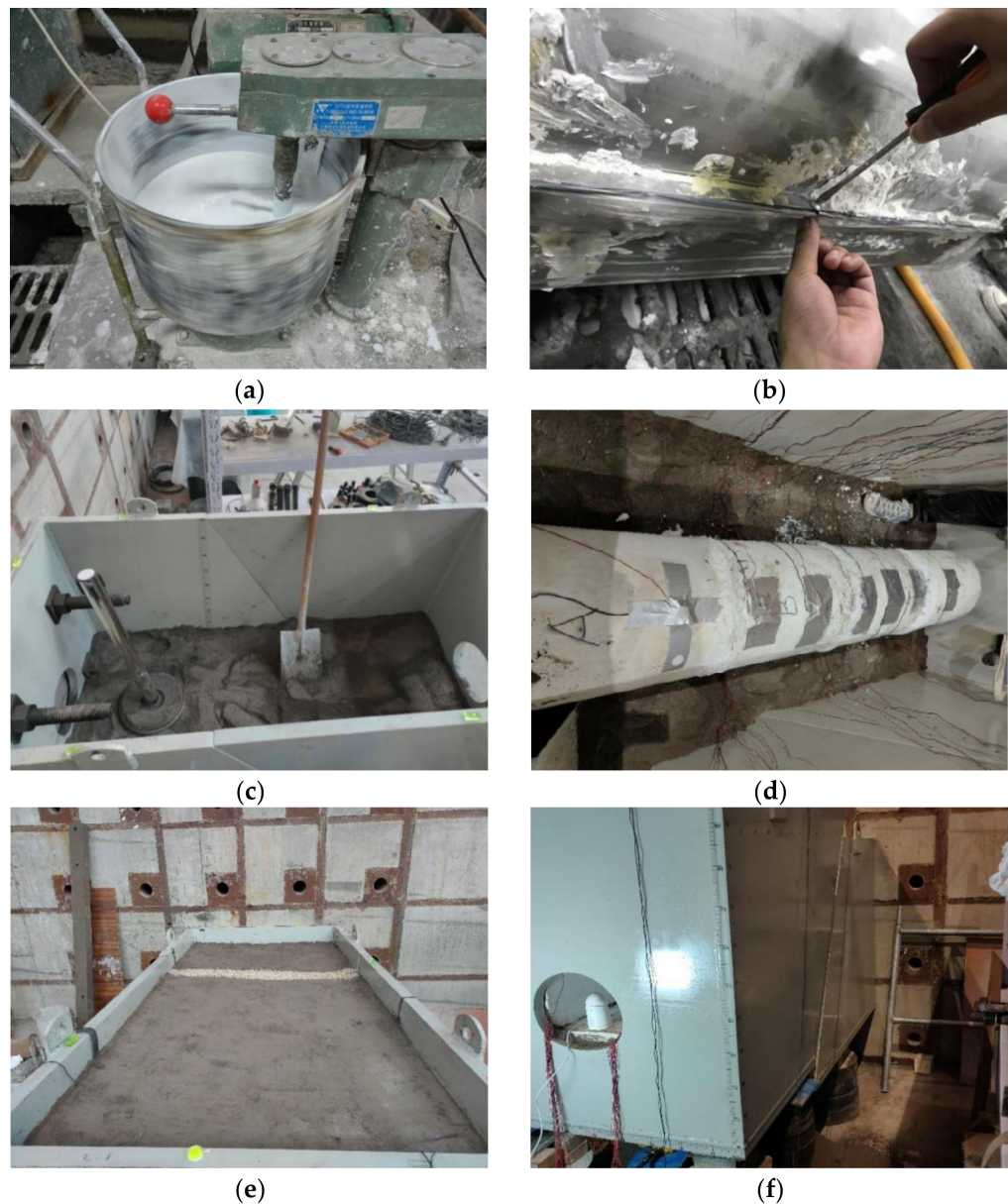
Figure 4. Steps of the mode stagger test: (**a**) Mixing of lining materials; (**b**) clamp and fix the mold; (**c**) compaction of surrounding rock materials; (**d**) put into the lining structure; (**e**) model box filling is completed; (**f**) stagger test.

2.5. Results of Model Test

2.5.1. Longitudinal Strain Analysis of Arch Waist of Lining

The hanging wall of the model box rose along the staggered surface under the action of the jack, and the surrounding rock interacted with the tunnel lining, resulting in the bending of the lining and a large difference in the longitudinal strain at the arch waist of the lining between the hanging wall and the footwall. The longitudinal strain distribution at the arch waist of the lining under different stagger distances is shown in Figure 5, in which the positive value is the tensile strain and the negative value is the compressive strain. It can be seen from the figure that the longitudinal tensile strain was mainly at the arch waist of the tunnel lining in the hanging wall and the fault fracture zone near the hanging wall, and the longitudinal strain at the arch waist of the tunnel lining in the footwall and the fault fracture zone near the footwall is mainly shown as compressive strain. With the increase in fault displacement, the longitudinal strain at the arch waist of the lining generally showed an upward trend, of which the maximum tensile strain was 151, which appeared at monitoring section 2, located in the hanging wall range, and was about 1.33 D away from the fault displacement surface (D is the tunnel diameter). The maximum compressive strain was −102, which occurred at monitoring section 4 and is located near the fault dislocation plane. If the influence of accidental factors is excluded, the maximum compressive strain of −49 appeared at monitoring section 5, located in the footwall range, and was about 0.67 D away from the fault dislocation surface.
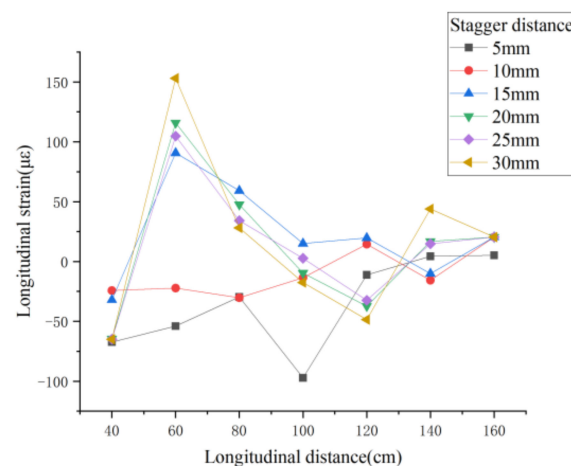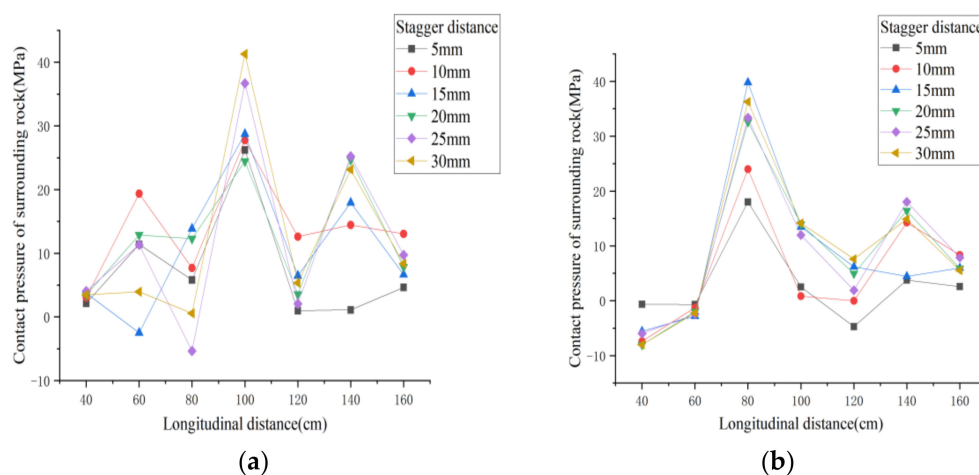

Figure 5. Longitudinal strain distribution of the arch waist.

According to the strain change law, the fault dislocation surface and the range of 1.5 D on both sides were the areas with the largest longitudinal strain change at the arch waist of the lining, while the areas far away were less affected by the fault dislocation. From the perspective of the strain variation amplitude, a drastic change occurred in the area where the fault dislocation surface was close to the hanging wall, and the change amplitude of the dislocation in the area where the fault dislocation surface was close to the footwall was small. It can be seen that the influence of fault dislocation on the tunnel in the hanging wall area was greater than that in the footwall area, and the area about 1.5 D near the hanging wall and about 0.5 D near the footwall of the fault dislocation surface should be considered the key area for the tunnel to resist dislocation.

2.5.2. Analysis of Contact Pressure of the Surrounding Rock

The dislocation distance of the fault and the subsequent mutual extrusion between the surrounding rock and the tunnel were the main reasons for the change of the contact pressure of the surrounding rock. It can be seen from Figure 6 that with the increase in the staggering distance of the hanging wall, the contact pressure of the surrounding rock at the vault and inverted arch of the tunnel showed an increasing trend. Under the forced movement of surrounding rock and lining structure, the larger value of surrounding rock

contact pressure was mainly concentrated in the fault dislocation surface and the range of 0.67 D near the hanging wall. The surrounding rock contact pressure in the footwall area was small and showed little change. The larger contact pressure of surrounding rock at the vault was concentrated in the range of 1.33 D on both sides of the fault dislocation surface, and the pressure was close to the maximum when the fault dislocation reached 30 mm. The larger value of the contact pressure of the surrounding rock at the inverted arch was concentrated in the range of 0.67 D near the hanging wall of the fault dislocation surface, and the pressure in other areas was small and changed little. The reason for the above phenomenon may be that the tunnel in the hanging wall area had an active upward trend due to the action of surrounding rock, so the contact pressure of the surrounding rock at the arch crown and inverted arch showed an increasing trend, and the value was large. The tunnel in the footwall area had a passive downward trend under the action of the surrounding rock, so the contact pressure of the surrounding rock at the arch crown and inverted arch showed an increasing trend, but the value and change range were small.


(**a**)　　　　　　　　　　　　　　　　(**b**)

Figure 6. Longitudinal distribution of surrounding rock contact pressure: (**a**) Vault; (**b**) inverted arch.

According to the change law of contact pressure of the surrounding rock, the fault dislocation surface and its 1.5 D range on both sides were the areas with the largest change of contact pressure between the lining and surrounding rock, and the areas far away were less affected by fault dislocation. From the perspective of the pressure change amplitude, violent changes occurred in the fault dislocation surface and the area near the hanging wall, and the change amplitude of the fault dislocation surface near the footwall was small. It can be seen that the influence of fault dislocation on the hanging wall area of the tunnel was greater than that of the footwall area. The inverted arch of the tunnel lining in the area where the fault dislocation surface was close to the hanging wall, at about 0.5 D, and the vault of the tunnel lining near the fault dislocation surface should be the key area for anti-dislocation fortification, which may be damaged earlier under fault activity.

2.5.3. Analysis of Lining Damage and Failure

From the perspective of the cracking morphology, the damage to the lining structure was mainly longitudinal cracking, which mainly occurred at the inverted arch and arch foot at 1.5 D of the fault and its nearby hanging wall area (D is the tunnel diameter). The oblique cracks at the arch waist were obvious. Based on the analysis of the change law of longitudinal strain and contact pressure of the surrounding rock, combined with the observed evolution characteristics of lining cracks, the approximate process of lining damage was analyzed, as shown in Figure 6. When the fault displacement reached 40 mm, mainly longitudinal cracking of a segment of the inverted arch occurred at first. With the increase in displacement, the cracks at the inverted arch develop upward to the arch foot and waist, mainly showing oblique cracks. Cracks lead to the stress release or transfer of nearby measuring points, which led to the serious impact of shear on the tunnel lining

structure near the fault dislocation surface. Figure 7a–c show the damage evolution of the lining; when the fault displacement reached 50 mm, the lining section showed a relative displacement, and the abutment staggering phenomenon occurred in the tunnel section of the fourth monitoring section. The closer to the fault dislocation position, the more the lining structure was seriously damaged. The abutment staggering phenomenon of the lining section is shown in Figure 7d.

(a)

(b)

(c)

(d)
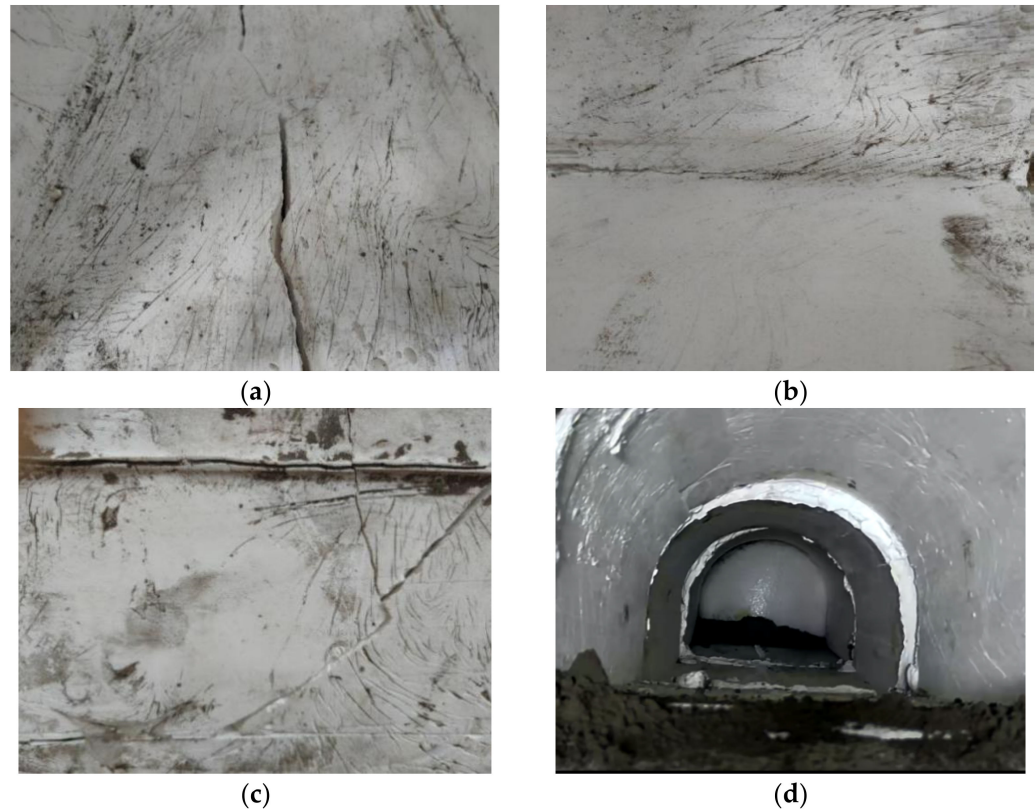
Figure 7. Schematic diagram of lining damage evolution: (**a**) Longitudinal cracks in the inverted arch; (**b**) longitudinal cracks in the arch foot; (**c**) oblique cracks in the arch waist; (**d**) segmental staggering.

3. Numerical Simulation

The model size was 30 m × 30 m × 60 m, as shown in Figure 8. The X direction is horizontal, the Y direction is vertical, and the Z direction is horizontal and longitudinal. The size parameters refer to the prototype enlarged by the model test at a similar scale. The models and parameters used in the surrounding rock and fault fracture zone can be seen in the previous section. The fault slip surface was simulated by viscous interface element coh3d8, which was located in the middle of the fault fracture zone. The primary support and secondary lining were also regarded as one, and the material was C30 concrete. The concrete damage plastic model (CDP model) was set and the segment length was 15 m, which is numbered as A, B, C, and D from the hanging wall to the footwall. Considering that the calculation model involves material nonlinearity and geometric nonlinearity, the element division method was structural mesh, and the element type adopted the eight node hexahedral full integral solid element c3d8, avoiding the default reduced integral c3d8r, which is conducive to calculation convergence. Similarly, in order to improve the calculation efficiency, the surrounding rock only adopted grid densification around the tunnel and at the fault fracture zone, and the whole length of the tunnel lining adopted a more refined grid. Table 4 shows the material physical and mechanical parameters of the model.

(**a**)   (**b**)
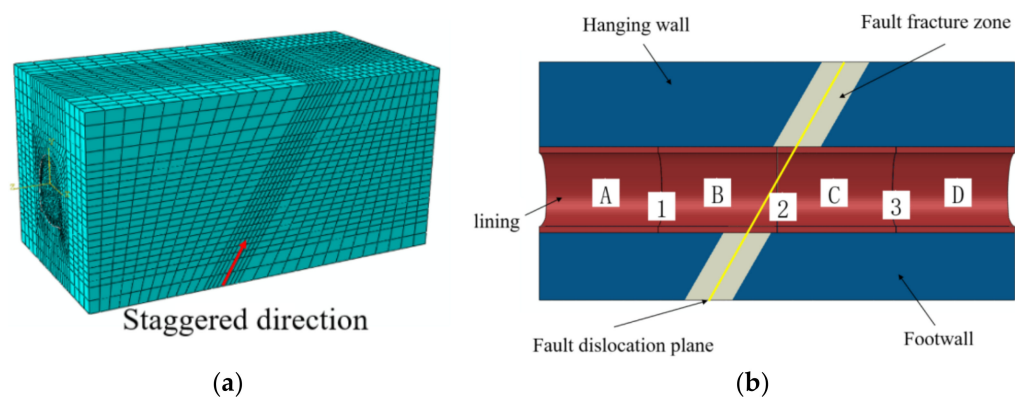
Figure 8. Numerical model: (**a**) Grid division and staggered diagram; (**b**) schematic diagram of a model section.

Table 4. Material physical and mechanical parameters.

Type	Density (kg/m^3)	Modulus of Elasticity E/(MPa)	Shear Modulus G/(MPa)	Poisson's Ratio ε (μ)	Cohesion c/(kPa)	Internal Friction Angle φ/(°)	Fracture Energy G/(N/m)
Surrounding rock	2100	4500	—	0.32	500	33	—
Fault	1900	1500	560	0.4	150	25	20
lining	2500	30,000	—	0.2	—	—	—

In order to simulate the relative slip and force transmission between the surrounding rock and lining in the process of fault dislocation, face-to-face contact was used in both places. The normal direction of the interface adopted hard contact; that is, the normal direction of the contact surface can transmit the contact pressure infinitely, but when the contact pressure is zero or negative, the contact surface is released and separated. Coulomb friction was used in the tangential direction of the interface. The following formula was used, and the penalty stiffness method was set. When the tangential contact stress reached the critical value, the relative slip occurred between the contact surfaces.

$$\tau = \mu P \tag{1}$$

In the equation, τ is the critical tangential contact stress, μ is the friction coefficient, and P is the normal contact pressure. The friction coefficient μ between lining sections was taken as 0.1, and three contact surfaces were set, numbered 1, 2, and 3, respectively. The friction coefficient μ between the surrounding rock and lining was taken as 0.4.

The analysis process of the simulation was divided into three steps:

(1) We constrained the normal displacement of the side and bottom of the model, the upper surface was a free surface, we killed the tunnel lining structural unit, and we applied gravity load to the surrounding rock structure to balance the in situ stress. Due to the Mohr-Coulomb constitutive model of surrounding rock and the existence of a fault fracture zone, the geostatic automatic geostress balance analysis in ABAQUS did not easily converge, so the OBD method was introduced here to realize geostress balance.

(2) The function of the life and death unit was to realize tunnel excavation and support, and the disturbance of tunnel excavation to the surrounding rock was not considered; that is, the construction length, excavation method, and support installation sequence were ignored, simplifying the process to one-step excavation and support.

(3) The pseudo static method was used to realize the fault dislocation; that is, to keep the footwall fixed, and apply the displacement along the fault dip direction to the hanging wall. The dislocation was controlled by the vertical displacement, so the dislocation refers to the vertical dislocation.

4. Comparison of Results

4.1. Maximum Principal Stress Analysis

Figures 9 and 10, respectively, show the cloud diagram of the maximum principal stress distribution of the lining and the maximum principal stress distribution curve of the lining at different parts. It can be seen that the absolute value of the maximum principal stress outside the vault and outside the arch waist increased with the increase in the fault dislocation distance, and extreme values mainly occurred within 10 m of both sides of the fault dislocation plane. The maximum principal stress on the outside of the lining vault, the outside of the arch waist, and the inside of the inverted arch was mainly tensile stress, but the outside of the vault near the hanging wall near the fault dislocation surface was prominently identified as compressive stress. It may be that the fault dislocation caused the compression at the vault of section B and C, which is the potential pressure damage area. The maximum principal stress on the inner side of the inverted arch was shown by the reduction in the fault dislocation surface from both ends to the middle, which can predict that the tensile damage will develop from the far end to the middle. The evolution law of arch crown cracks in model tests was verified.
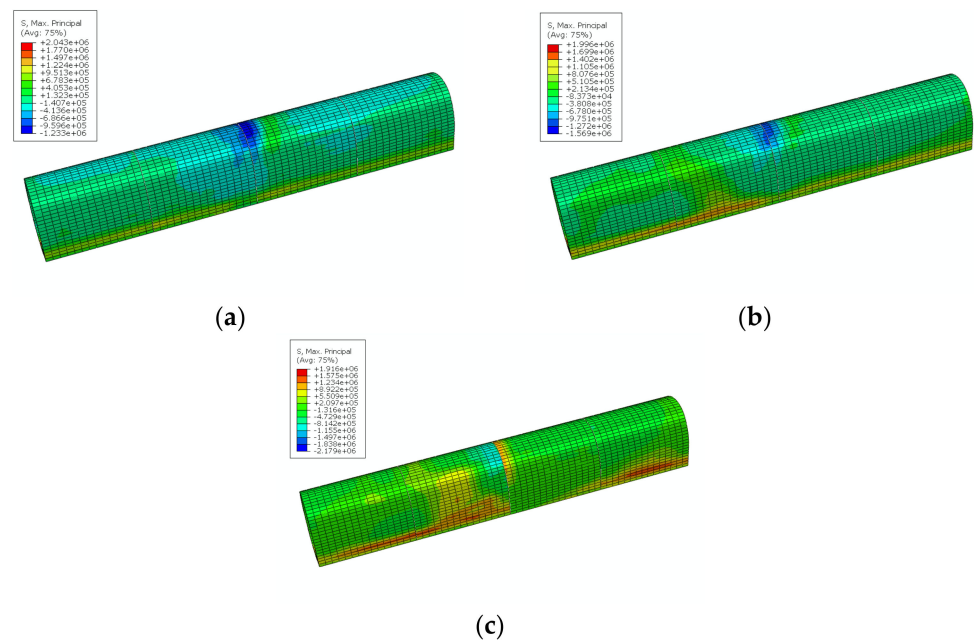

(a)

(b)

(c)

Figure 9. Cloud diagram of lining maximum principal stress distribution: (**a**) Stagger distance 1 cm; (**b**) stagger distance 3 cm; (**c**) stagger distance 5 cm.
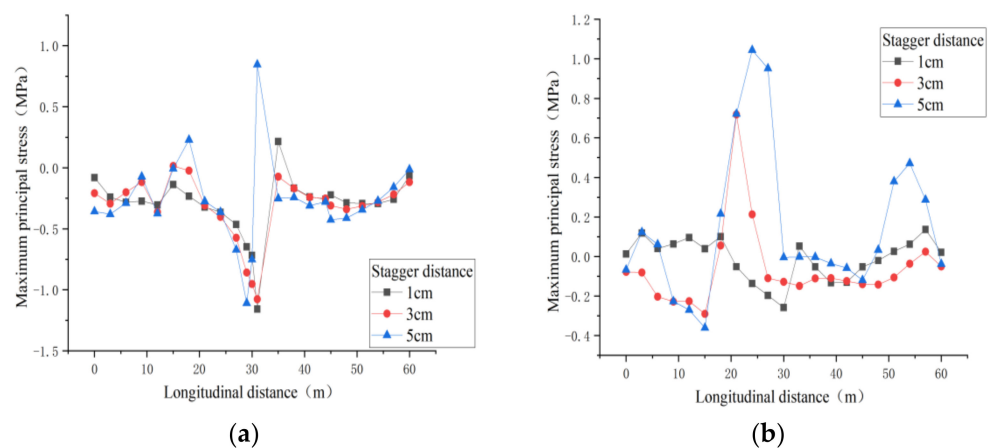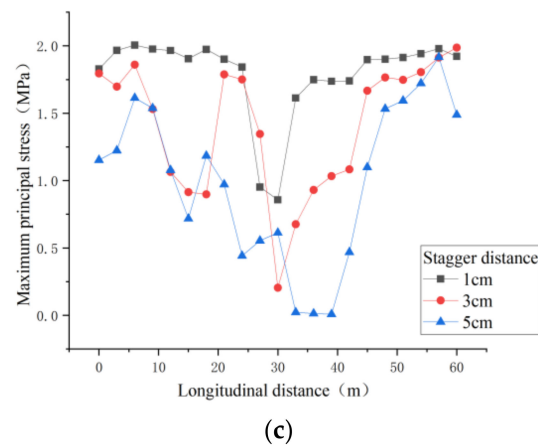

(a)

(b)

Figure 10. *Cont*.

(**c**)

Figure 10. Distribution curves of the maximum principal stress in different parts of lining: (**a**) Outside of vault; (**b**) outside the arch waist; (**c**) inside of inverted arch.

4.2. Longitudinal Stress Analysis

Figures 11 and 12, respectively, show the overall longitudinal stress distribution of the lining and the longitudinal distribution of different parts of the lining under different stagger distances. With the outermost axis of the hanging wall as the coordinate zero point of the longitudinal distance, the fault dislocation plane passed through the longitudinal center of the tunnel. It can be seen from the figure that the longitudinal stress of the lining was mainly compression, and with the increase in the dislocation distance, the longitudinal stress of each part of the lining also increased. The extreme value of longitudinal stress at the vault was mainly located in the range of 5~10 m near the footwall direction of the fault dislocation surface. The extreme value of longitudinal stress at the arch waist was mainly located in the range of 5~10 m on both sides of the fault dislocation surface, and the extreme value appeared near the hanging wall, which was close to the distribution law of longitudinal strain at the arch waist in the model test. The extreme value of longitudinal stress at the inverted arch was mainly located in the range of 10~15 m near the hanging wall direction of the fault dislocation surface. When the fault dislocation distance was 5 cm, the extreme value of compressive stress in each part did not reach the complete failure strength.

With the increase in fault dislocation distance, within the hanging wall range, the absolute value of longitudinal stress increased gradually within the range of about 10 m near the fault dislocation surface at the vault, while the longitudinal stress changed non-significantly in other ranges. The overall longitudinal compressive stress in the arch waist showed an increasing trend, and the closer it was to the fault dislocation surface, the greater the absolute value. The longitudinal stress of the inverted arch was mainly compression and showed an increasing trend. Within the footwall, the longitudinal compressive stress of the vault and the waist of the arch generally showed an upward trend, while the longitudinal stress of the inverted arch did not change significantly, but it showed a tensile trend.

By comparing the distribution and variation of the longitudinal strain at the arch waist of the lining surface with the fault dislocation distance in the model test, we found that it was basically consistent with the numerical simulation law.

4.3. Contact Pressure Analysis

It can be seen from Figures 13 and 14 that with the increase in fault dislocation distance, the contact pressure of surrounding rock at the arch crown and inverted arch mainly showed an increasing trend. The maximum contact stress of the surrounding rock at the vault occurred within 5 m of the staggered surface near the hanging wall area, the smaller value was concentrated in the footwall area of the tunnel, and it tended to be stable with the increase in longitudinal distance. This showed that the influence of fault dislocation on the hanging wall of the tunnel was significantly greater than that on the footwall.
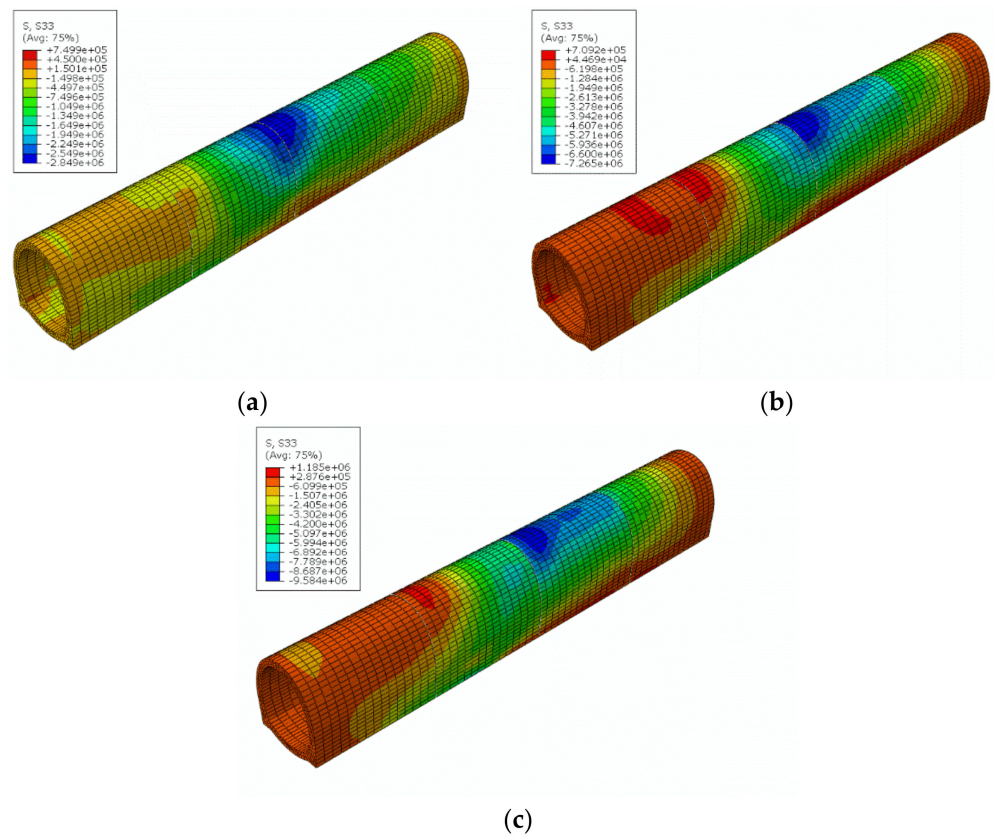
(**a**)

(**b**)

(**c**)

Figure 11. Lining overall longitudinal stress distribution cloud map: (**a**) Stagger distance 1 cm; (**b**) stagger distance 3 cm; (**c**) stagger distance 5 cm.

(**a**)
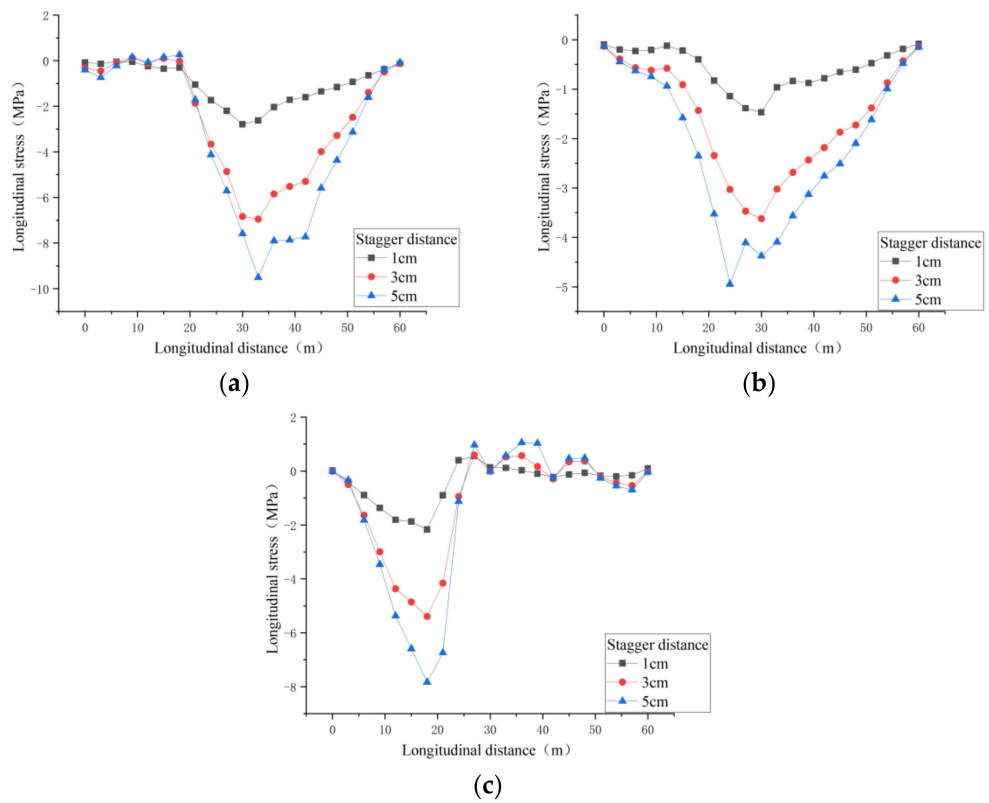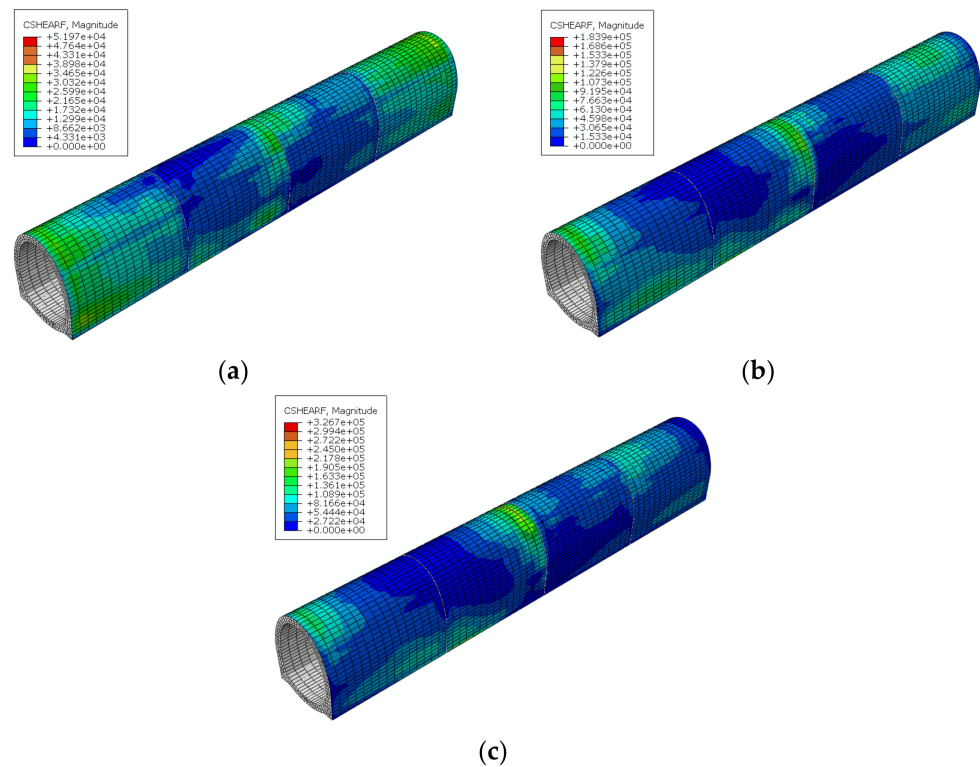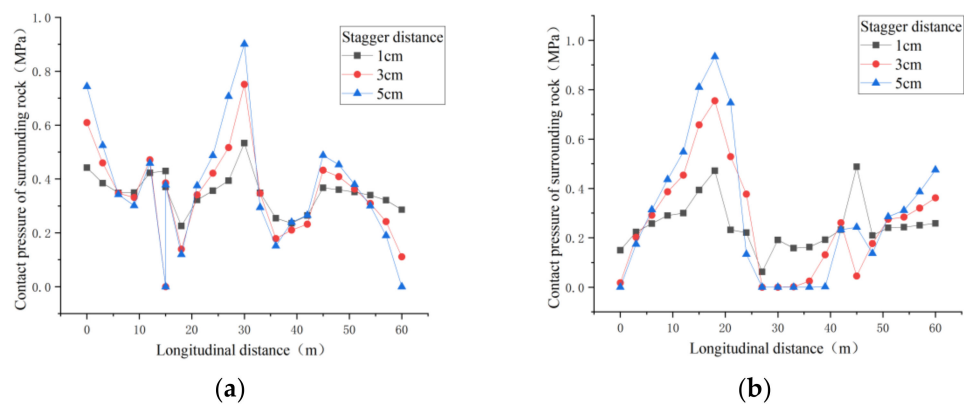
(**b**)

(**c**)

Figure 12. Longitudinal stress distribution curve of different parts of lining: (**a**) Outside of vault; (**b**) outside the arch waist; (**c**) inside of inverted arch.

(a)

(b)

(c)

Figure 13. Cloud diagram of the surrounding rock contact pressure distribution on the lining surface: (**a**) Stagger distance 1 cm; (**b**) stagger distance 3 cm; (**c**) stagger distance 5 cm.


(a)

(b)

Figure 14. The contact pressure of the surrounding rock along the longitudinal distribution curve of the tunnel: (**a**) Vault; (**b**) inverted arch.

Figure 15 shows the contact pressure distribution of the lining segment contact surface 2 intersecting the fault dislocation surface. When the fault began to stagger, the contact pressure was mainly concentrated in the area above the arch waist, and the closer it was to the arch crown, the greater the pressure. With the increase in stagger distance, the contact pressure continued to increase and spread downward, indicating that the squeezing effect between lining segments B and C was increasing. When the staggering distance reached 5 cm, the extreme value of contact pressure was 9.459 MPa, located at the arch crown, and the distribution range occupied all the areas above the arch foot, while no contact pressure was generated at the inverted arch. The reason for this may be that under the influence of fault dislocation, the abutment staggering phenomenon occurs between lining segments, and the contact surface of the inverted arch may have been pulled apart. Figure 16 shows the displacement of the lining section with a stagger distance of 5 cm. The maximum displacement reached 6 cm, and the relative displacement near the contact surface of sections B and C was about 1.5 cm.
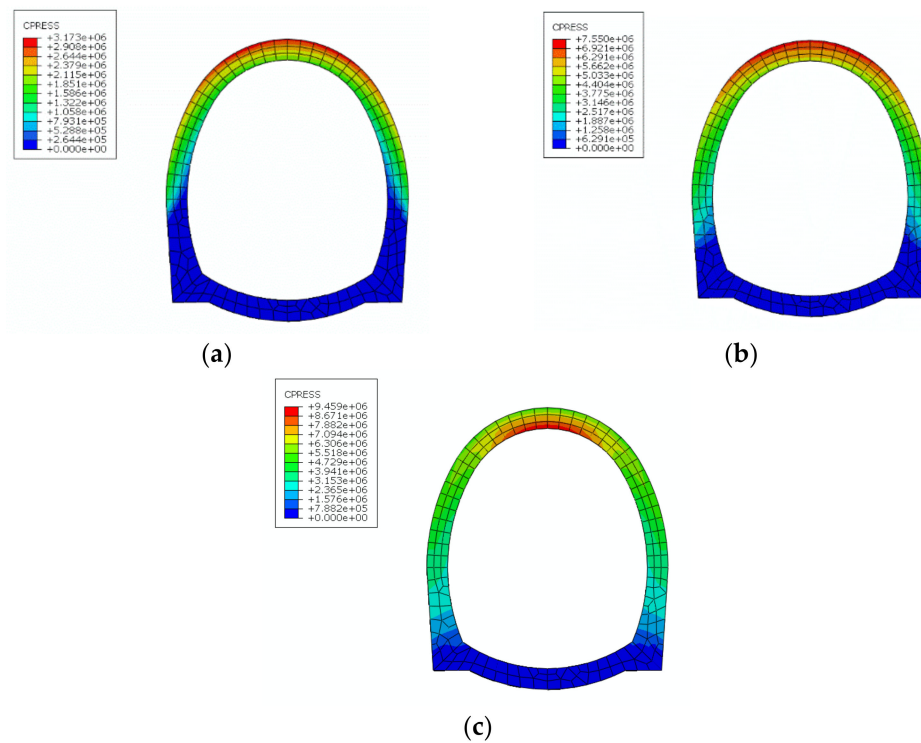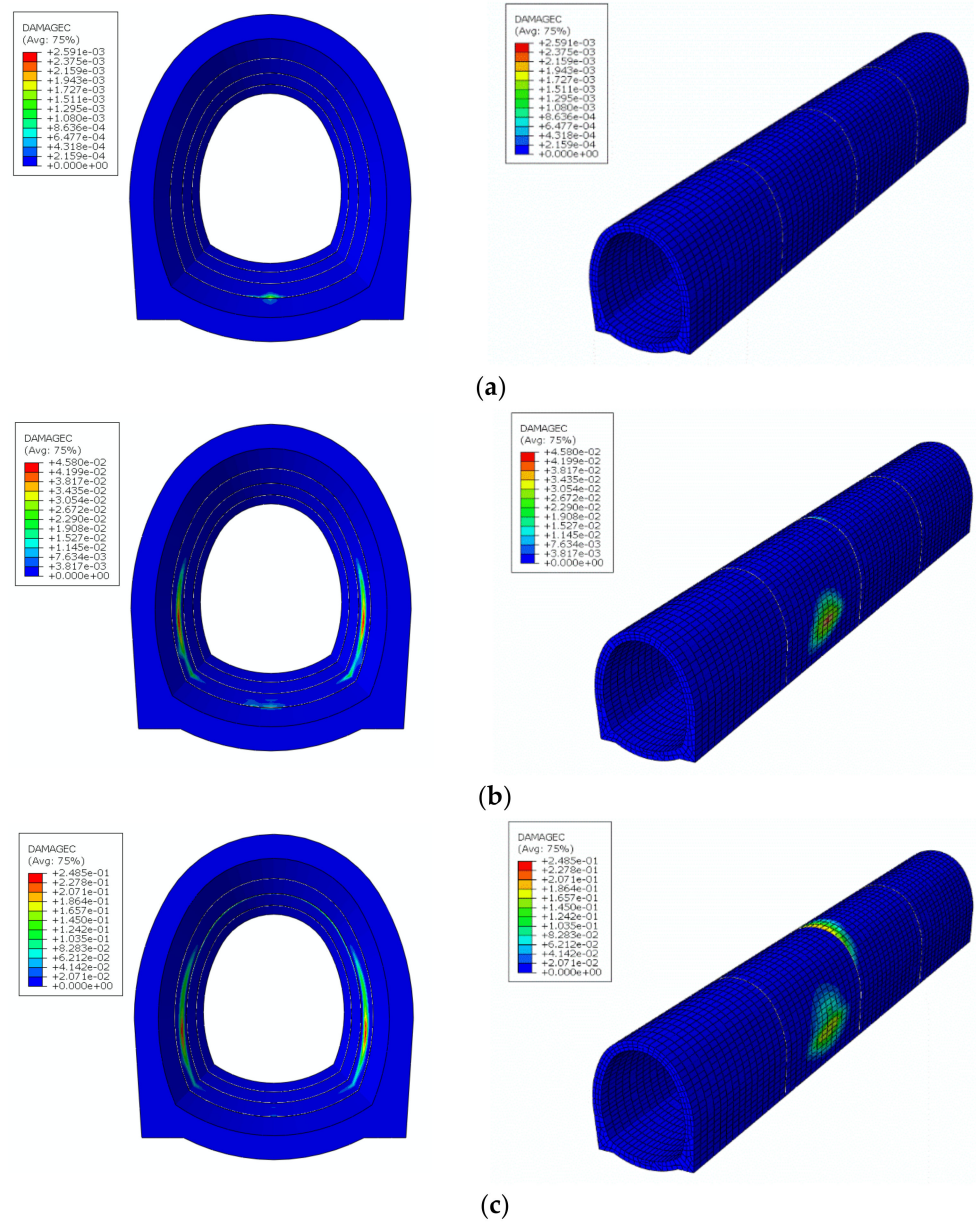
Figure 15. Contact pressure evolution of the lining segment contact surface 2: (**a**) Stagger distance 1 cm; (**b**) stagger distance 3 cm; (**c**) stagger distance 5 cm.
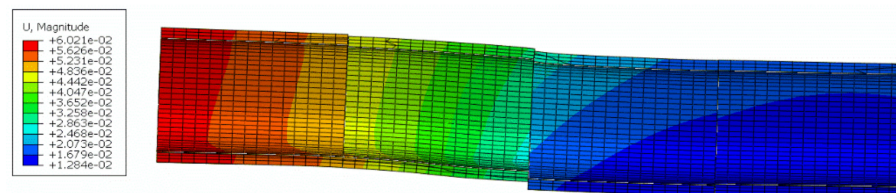

Figure 16. Displacement cloud map of the lining segment when the dislocation distance was 5 cm (magnified 50 times).

It can be seen from Figure 17 that the pressure damage of the lining was mainly concentrated in the range of 15~20 m near the fault dislocation surface. With the increase in the dislocation distance, the pressure damage first appeared on the contact surface of each section, and the dislocation separation occurred on the contact surface, and the pressure damage gradually transferred to the inner and outer sides of the arch waist and the outer side of the arch crown. When the staggering distance was 5 cm, the extreme value of compressive damage was 0.2485 (0~1 indicates the degree of damage), which occurred at the inner side of the arch waist of section B close to the staggering surface, and at the outer side of the arch crown of section C close to the staggering surface. Figure 18 shows that the tensile damage was mainly located in the inverted arch. At first, the tensile damage appeared on the front and rear sides of the segment contact surface 1. With the increase in the staggering distance, the tensile damage gradually developed to segment A and segment B, and the extreme value also increased. When the dislocation distance was 5 cm, the tensile damage had penetrated the inverted arch of section B, reaching the fault dislocation surface area, and the extreme value was 0.9517, which was close to complete damage. At this point, the conjecture about the contact pressure at the inverted arch of the contact surface of the lining section in the previous section was verified, and the tension damage also occurred at the inner side of the arch waist of section B. The damage degree was between 0.2 and 0.3. Comparing the phenomena of the lining crack area and segment staggering in the model test, they were basically consistent with the law of numerical simulation.

(**a**)

(**b**)

(**c**)

Figure 17. Compression damage evolution of the lining: (**a**) Stagger distance 1 cm; (**b**) stagger distance 3 cm; (**c**) stagger distance 5 cm.

(**a**)
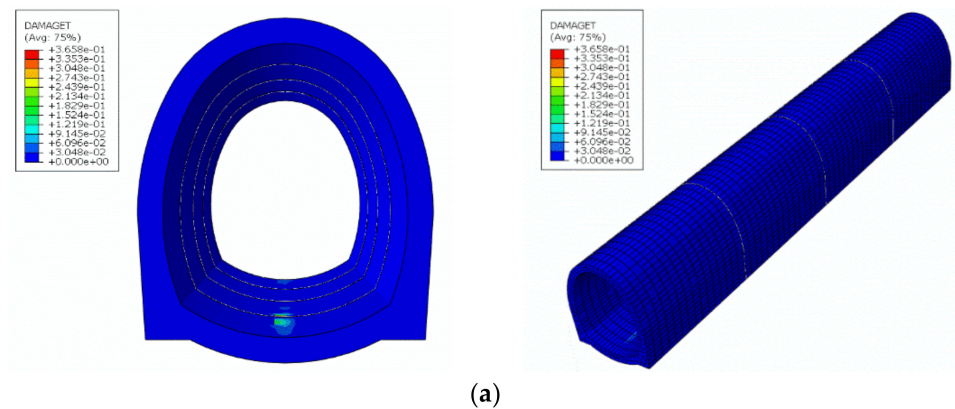
Figure 18. *Cont.*
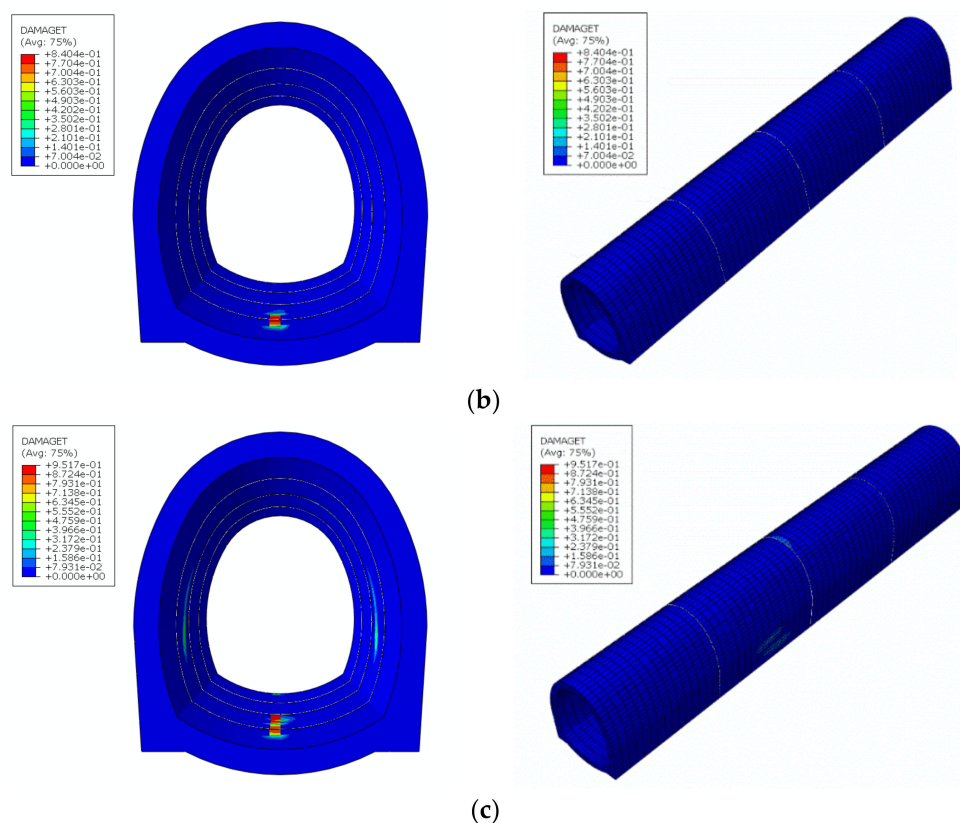
Figure 18. Tensile damage evolution of the lining: (**a**) Stagger distance 1 cm; (**b**) stagger distance 3 cm; (**c**) stagger distance 5 cm.

4.4. Verification Result Analysis

(1) The staggered distances of 1 cm and 3 cm were analyzed by numerical simulation. The maximum principal stress values of the outer side of the tunnel crown, the outer side of the arch waist, and the inner side of the inverted arch under the condition of 5 cm were obtained. The evolution law of the cracks in the arch crown in the model test was verified.

(2) The staggered distances of 1 cm and 3 cm were analyzed by numerical simulation. Longitudinal stress values of the outer side of the tunnel crown, the outer side of the arch waist, and the inner side of the inverted arch under the condition of 5 cm were obtained. The distribution and variation of the longitudinal strain at the arch waist of the lining surface with the displacement distance of the fault in the model test were compared, and they were basically consistent with the numerical simulation law.

(3) The staggered distances of 1 cm and 3 cm were analyzed by numerical simulation. Longitudinal stress of the outer side of the tunnel crown, the outer side of the arch waist, and the inner side of the inverted arch under the condition of 5 cm were obtained.

5. Conclusions

5.1. Summary of Main Research Contents

Based on a railway tunnel crossing an active reverse fault, this paper used the methods of literature analysis, model test, numerical simulation, and statistical analysis for this research. First, based on the similarity theorem, we carried out similar material tests, and designed and completed reverse fault dislocation model tests. Secondly, ABAQUS was used to establish a three-dimensional numerical calculation model, and the effectiveness of the numerical simulation was verified by comparing the model test results. The main conclusions are as follows:

(1) Through an orthogonal test, the proportioning design of similar materials of the surrounding rock was carried out, a range analysis of the results was carried out, and the influence trend diagram of the river sand particle size combination, river sand content, and fly ash content on material cohesion and the internal friction angle was obtained. We found that the influence of the river sand particle size combination on cohesion was four times that of the river sand content and fly ash content, and the appropriate proportion of similar materials of the surrounding rock was obtained. According to the data fitting, when the retarder content was 0.5%, the relationship formula between the proportion of gypsum and water and the elastic modulus could be obtained, and the appropriate proportion of similar lining materials was determined. This provides reference and guidance for the configuration of similar materials for model tests in the future.

(2) Through the model test, it was found that the deformation and failure of the tunnel lining structure were mainly concentrated in and near the fault fracture zone in the reverse fault dislocation. The influence range of the footwall was about 0.5 D (D is the tunnel diameter), and that of the hanging wall was about 1.5 D. The damage continued to accumulate with the increase in dislocation. The influence of fault dislocation on the tunnel in the hanging wall area was greater than that of the footwall, and the maximum surrounding rock pressure and the maximum longitudinal strain appeared in the hanging wall of the tunnel. The lining structure at the fault and near the hanging wall was damaged to a large extent, and there were inclined cracks and transverse and longitudinal cracks on the inner wall of the lining structure, and the abutment staggering phenomenon occurred at the fault along the longitudinal direction of the tunnel. Therefore, the reinforcement of the arch foot and arch waist should be strengthened at the position of the tunnel close to the fault to improve its shear resistance, while the flexible deformation capacity of the connecting material should be enhanced at the connection of the tunnel sections to improve its fault resistance.

(3) The numerical simulation results were compared with the model test results to verify the effectiveness of both. Based on this, a three-dimensional simulation method of reverse fault dislocation based on a viscous interface model for railway tunnels is proposed.

5.2. Research Deficiencies and Future Prospects

(1) Due to the limitations of test conditions and time, the model test simplified the tunnel prototype to varying degrees, failed to fully consider the impact of the model boundary on the tunnel, and simplified the tunnel lining support form into one. The above simplified design will have different degrees of impact on the test results. It is hoped that in future research, funding and time factors will allow model similarity to be achieved to the greatest extent.

(2) Only the damage behavior of the tunnel lining structure under the dislocation of the reverse fault was analyzed and studied. In fact, the typical fault activity forms also include normal faults and strike slip faults, and the damage behavior of the tunnel lining structure under atypical combined fault forms needs to be further studied.

(3) In the model test and numerical simulation, the surrounding rock and fault were treated as a single uniform medium, and the different distribution of the surrounding rock material properties and surface characteristics in the stratum were not considered. Further analysis and research are needed to ascertain the impact this may have had on the results.

(4) The sensitivity analysis of the influencing factors only used the damage extreme value, so the evaluation of the overall damage of the lining was not comprehensive enough. In future, the damage index of the overall lining under tension and compression should be introduced for further study.

Author Contributions: Conceptualization, H.S. and Z.Z.; methodology, K.M.; software, H.S.; validation, Z.Z.; formal analysis, H.S. and Z.Z.; investigation, S.Z.; resources, Z.Z.; data curation, H.S.; writing—original draft preparation, K.M.; writing—review and editing, S.Z.; visualization, Z.Z.; supervision, H.S. All authors have read and agreed to the published version of the manuscript.

Conflicts of Interest: The authors declare no conflict of interest.

References

1. Elshaboury, N.; AlSakkaf, A.; Mohammed, A. Construction and Demolition Waste Management Research: A Science Mapping Analysis. *Int. J. Environ. Res. Public Health* **2022**, *19*, 4496. [CrossRef] [PubMed]
2. Yuan, B.; Chen, W.; Zhao, J. The Effect of Organic and Inorganic Modifiers on the Physical Properties of Granite Residual Soil. *Adv. Mater. Sci. Eng.* **2022**, *2022*, 9542258. [CrossRef]
3. Abdelkader, E.; AlSakkaf, A.; Elshaboury, N. Hybrid Grey Wolf Optimization-Based Gaussian Process Regression Model for Simulating Deterioration Behavior of Highway Tunnel Components. *Processes* **2021**, *10*, 36. [CrossRef]
4. Yuan, B.; Li, Z.; Chen, W. Influence of Groundwater Depth on Pile–Soil Mechanical Properties and Fractal Characteristics under Cyclic Loading. *Fractal Fract.* **2022**, *6*, 198. [CrossRef]
5. Yuan, B.; Chen, M.; Chen, W. Effect of Pile-Soil Relative Stiffness on Deformation Characteristics of the Laterally Loaded Pile. *Adv. Mater. Sci. Eng.* **2022**, *2022*, 4913887. [CrossRef]
6. Sun, F. Study on Anti Dislocation Mechanism and Method of Tunnel Crossing Active Fault Mountains. Ph.D. Thesis, Beijing Jiaotong University, Beijing, China, 2018.
7. Wang, H.; Liu, X.; Li, N.; Xie, D. Study on safety evaluation and reinforcement of longitudinal crack tunnel lining structure. *J. Rock Mech. Eng.* **2010**, *29*, 2651–2656.
8. Qi, B.; Wang, F.; Chen, J. Numerical simulation of structural response of tunnel crossing fault under stick slip fault dislocation. *Build. Struct.* **2020**, *50*, 753–758.
9. Xiao, Z. Research on Deformation and Failure of Soil Tunnel under Strike Slip Fault Dislocation. Master's Thesis, Overseas Chinese University, Quanzhou, China, 2019.
10. Liu, Y.; Lai, J.; Xin, J.; Li, X.; Xing, R. Dynamic comparative experimental study on Seismic Response Law of tunnel crossing fault. *Geotech. Mech.* **2019**, *40*, 4693–4702.
11. Liu, X.; Wang, X.; Lin, L. Experimental analysis of the influence of 45° dip normal fault stick slip dislocation on the tunnel. *J. Tongji Univ. Nat. Sci. Ed.* **2014**, *42*, 44–50.
12. Liu, X.; Wang, X.; Lin, L. Experimental study on the influence of 60° dip normal fault stick slip dislocation on mountain tunnel. *J. Civ. Eng.* **2014**, *47*, 121–128.
13. Liu, X.; Wang, X.; Lin, L. Model test study on the influence of 75° dip normal fault stick slip dislocation on highway tunnel. *J. Rock Mech. Eng.* **2013**, *32*, 1714–1720.
14. Zhang, Y.; Chen, X.; Yuan, Z. Influence of fault dislocation on cross fault tunnel. *J. Nanjing Univ. Technol. Nat. Sci. Ed.* **2019**, *41*, 129–134.
15. Baziar, M.H.; Nabizadeh, A.; Lee, C.J.; Hung, W.Y. Centrifuge modeling of interaction between reverse faulting and tunnel. *Soil Dyn. Earthq. Eng.* **2014**, *65*, 151–164. [CrossRef]
16. Kiani, M.; Akhlaghi, T.; Ghalandarzadeh, A. Experimental modeling of segmental shallow tunnels in alluvial affected by normal faults. *Tunn. Undergr. Space Technol. Inc. Trenchless Technol. Res.* **2016**, *51*, 108–119. [CrossRef]
17. Sabagh, M.; Ghalandarzadeh, A. Centrifugal modeling of continuous shallow tunnels at active normal faults intersection. *Transp. Geotech.* **2020**, *22*, 100325. [CrossRef]
18. Saiyar, M.S.; Take, W.A.; Moore, I.D. Post-failure fracture angle of brittle pipes subjected to differential ground movements. *Tunn. Undergr. Space Technol. Inc. Trenchless Technol. Res.* **2015**, *49*, 114–120. [CrossRef]
19. Fu, J.; Xie, J.; Yang, J. *The Effects of Local Cavities on the Cracking Performance of an Existing Tunnel Lining*; Springer: Cham, Switzerland, 2018.
20. Geng, Y.; Zhu, Z.; Gu, G.; Zhang, C. An Analysis of the Effects of Cavities in Different Positions Behind the Tunnel Lining under the Action of an Earthquake. *Traffic Eng. Technol. Natl. Def.* **2016**, *14*, 37–40.
21. Kim, M.-J.; Park, T.-G. A Case Study on Crack Control of Tunnel Lining through Construction Example. *Proc. Korean Concr. Soc. Acad. Conf.* **2017**, *29*, 409–410.
22. Fang, Y.; Guo, J.; Kang, H. Influence of voids behind lining on the mechanical behavior of lining structure of highway tunnel in watery strata. *Chin. J. Rock Mech. Eng.* **2016**, *35*, 1648–1658.
23. Su, J.; Jie, Y.; Niu, X. Mechanical Behavior of Tunnel Lining with Cracks at Different Positions. *Symmetry* **2020**, *12*, 194. [CrossRef]
24. Jin, M.; Liu, X.; Zhong, Z. Model Test Research on the Mechanical Characteristics of Tunnel Lining Structures under Local High Water Pressure in Concealed Karsts. *IOP Conf. Ser. Earth Environ. Sci.* **2021**, *861*, 022010. [CrossRef]
25. Chen, Z.; Bian, M. Dynamic Centrifuge Test and Numerical Modelling of the Seismic Response of the Tunnel in Cohesive Soil Foundation. *Buildings* **2022**, *12*, 337. [CrossRef]

26. Qiao, Y.; Tang, J.; Liu, G. Longitudinal mechanical response of tunnels under active normal faulting. *Undergr. Space* **2022**, *7*, 662–679. [CrossRef]

27. An, S.; Tao, L.J.; Han, X.C.; Zhang, Y. Application of two-level design method on subway tunnel crossing active fault: A case study on Urumqi subway tunnel intersected by reverse fault dislocation. *Bull. Eng. Geol. Environ.* **2021**, *80*, 3871–3884. [CrossRef]